Anisotropy in cohesive, frictional granular media

2005 J. Phys.: Condens. Matter 17 S2623

(http://iopscience.iop.org/0953-8984/17/24/017)

INSTITUTE OF PHYSICS PUBLISHING JOURNAL OF PHYSICS: CONDENSED MATTER

J. Phys.: Condens. Matter **17** (2005) S2623–S2640 doi:10.1088/0953-8984/17/24/017

Anisotropy in cohesive, frictional granular media

Stefan Luding

Particle Technology, DelftChemTech, TUDelft, Julianalaan 136, 2628 BL Delft, The Netherlands

E-mail: s.luding@tnw.tudelft.nl

Received 16 March 2005
Published 3 June 2005
Online at stacks.iop.org/JPhysCM/17/S2623

Abstract

The modelling of cohesive, frictional granular materials with a discrete particle molecular dynamics is reviewed. From the structure of the quasi-static granular solid, the fabric, stress, and stiffness tensors are determined, including both normal and tangential forces. The influence of the material properties on the flow behaviour is also reported, including relations between the microscopic attractive force and the macroscopic cohesion as well as the dependence of the macroscopic friction on the microscopic contact friction coefficient. Related to the dynamics, the anisotropy of both structure and stress are exponentially approaching the maximum.

1. Introduction

The microscopic understanding of the macroscopic material behaviour of granular materials such as sand or powder is one of today's great challenges in material science and physics. Granular media are discontinuous, inhomogeneous, disordered, and anisotropic on a 'microscopic' scale, and their behaviour is usually intermittent, nonlinear and history dependent. Nevertheless, continuum models are applied in large scale industrial design of, for example, silos, where the models are based on constitutive relations and often on experimental observations and empirical assumptions.

The rich phenomenology observed in granular matter is due to the changing contact network of the structure formed by the grains, but also due to the inhomogeneous stress distribution in granular assemblies and the corresponding force networks. There are always large fluctuations of contact forces and a reorganization of the network due to deformations typically leads to a restructuring of those. When an initially isotropic contact network is deformed, the result is likely to be anisotropic. Translating this 'microscopic' information all the way up to a macroscopic description, via a so-called micro–macro model, is one issue of this paper.

We do not review all the existing literature in this field here; rather we point the reader's attention to the books by [1–3] and some references by various groups [4–14] and the references therein. Parts of the results presented here were already published in [10, 14, 15].

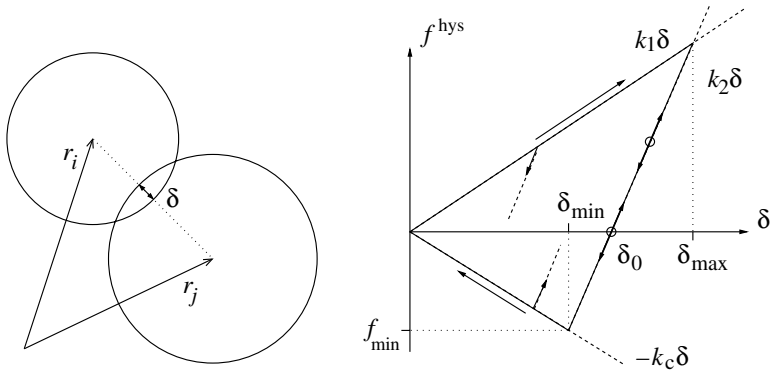

Figure 1. Left: two-particle contact with overlap δ. Right: force displacement relation with three material parameters k_1, k_2, and k_c.

In the following, a micro–macro averaging formalism is presented, based on single contact information [14], and the numerical method of molecular dynamics (MD), also called the discrete element method (DEM), see for example [7, 14–16], is applied in order to obtain the macroscopic constitutive relations. The behaviour of the stress, fabric, and stiffness tensors under shear is discussed for different microscopic material parameters.

2. Simulation details

The discrete element model (DEM) [1, 2, 7, 16–21] is briefly introduced in this section; for more details see [10, 14, 15, 22–24] and the references therein. However, before going into numerical details, the model system is described.

2.1. Discrete particle model

The elementary units of granular materials are mesoscopic grains which deform under stress. Since the realistic modelling of the deformations of the particles is much too complicated, we relate the normal interaction force to the overlap δ of two circular particles; see figure 1.

If all forces $\boldsymbol{f}_i$ acting on particle i, either from other particles, from boundaries or from external forces, are known, the problem is reduced to the integration of Newton's equations of motion for the translational and rotational degrees of freedom

$$m_i \frac{\mathrm{d}^2}{\mathrm{d}t^2}\boldsymbol{r}_i = \boldsymbol{f}_i, \qquad \text{and} \qquad I_i \frac{\mathrm{d}^2}{\mathrm{d}t^2}\varphi_i = \boldsymbol{t}_i \tag{1}$$

with the mass m_i of particle i, its position $\boldsymbol{r}_i$, the total force $\boldsymbol{f}_i = \sum_{\rm c} \boldsymbol{f}_i^c$ acting on it due to contacts with other particles or with the walls, its moment of inertia I_i, its angular velocity $\omega_i = \mathrm{d}\varphi_i/\mathrm{d}t$ and the total torque $\boldsymbol{t}_i = \sum_{\rm c} \boldsymbol{l}_i^c \times \boldsymbol{f}_i^c$.

2.1.1. Linear normal contact law. Two particles i and j interact only if they are in contact so that their overlap,

$$\delta = (a_i + a_j) - (\boldsymbol{r}_i - \boldsymbol{r}_j)\cdot\boldsymbol{n}, \tag{2}$$

is positive, with the unit vector $\boldsymbol{n} = \boldsymbol{n}_{ij} = (\boldsymbol{r}_i - \boldsymbol{r}_j)/|\boldsymbol{r}_i - \boldsymbol{r}_j|$ pointing from j to i.

The force on particle i, from particle j can be decomposed into a normal and a tangential part, where the simplest normal force is a linear spring and a linear dashpot

$$f_i^n = k\delta + \gamma_0\dot{\delta}, \tag{3}$$

with spring constant k and some damping coefficient γ_0. The half-period of a vibration around the equilibrium position can be computed, and one obtains a typical response time $t_c = \pi/\omega$, with $\omega = \sqrt{(k/m_{ij}) - \eta_0^2}$ the eigenfrequency of the contact, the reduced mass $m_{ij} = m_i m_j/(m_i + m_j)$, and the rescaled damping coefficient $\eta_0 = \gamma_0/(2m_{ij})$. The energy dissipation during a collision, as caused by the dashpot, leads to a restitution coefficient $r = -v_n'/v_n = \exp(-\eta_0 t_c)$, where the prime denotes the normal velocity after a collision. For a more detailed discussion of this and other, more realistic, nonlinear contact models see for example [15, 25].

The contact duration t_c is also of practical technical importance, since the integration of the equations of motion is stable only if the integration time-step Δt_{MD} is much smaller than t_c. Since t_c depends on the magnitude of dissipation, in the extreme case of an overdamped spring, it can become very large. Therefore, the use of neither too weak nor too strong dissipation is recommended.

2.1.2. Cohesive (hysteretic) normal contact model. Here we apply a variant of the linear hysteretic spring model [15, 22, 25–27], as an alternative to the frequently applied spring–dashpot models. This model is the simplest version of some more complicated nonlinear hysteretic force laws [26, 28, 29], which reflect the fact that, at the contact point, plastic deformations may take place. The repulsive (hysteretic) force can be written as

$$f^{\mathrm{hys}} = \begin{cases} k_1\delta & \text{for loading,} & \text{if } k_2(\delta - \delta_0) \geqslant k_1\delta \\ k_2(\delta - \delta_0) & \text{for un/reloading,} & \text{if } k_1\delta > k_2(\delta - \delta_0) > -k_c\delta \\ -k_c\delta & \text{for unloading,} & \text{if } -k_c\delta \geqslant k_2(\delta - \delta_0) \end{cases} \tag{4}$$

with $k_1 \leqslant k_2$; see figure 1.

During the initial loading the force increases linearly with the overlap δ, until the maximum overlap $\delta_{\max}$ is reached (which has to be kept in memory as a history parameter). The line with slope k_1 thus defines the maximum force possible for a given δ. During unloading the force drops from its value at $\delta_{\max}$ down to zero at overlap $\delta_0 = (1 - k_1/k_2)\delta_{\max}$, on the line with slope k_2. Reloading at any instant leads to an increase of the force along this line, until the maximum force is reached; for still increasing δ, the force again follows the line with slope k_1, and $\delta_{\max}$ has to be adjusted accordingly.

Unloading below δ_0 leads to negative, attractive forces until the minimum force $-k_c\delta_{\min}$ is reached at the overlap $\delta_{\min} = (k_2 - k_1)\delta_{\max}/(k_2 + k_c)$. This minimum force, i.e. the maximum attractive force, is obtained as a function of the model parameters k_1, k_2, k_c, and the history parameter $\delta_{\max}$. Further unloading leads to attractive forces $f^{\mathrm{hys}} = -k_c\delta$ on the cohesive branch with slope $-k_c$. The highest possible attractive force, for given k_1 and k_2, is reached for $k_c \to \infty$, so that $f_{\max}^{\mathrm{hys}} = -(k_2 - k_1)\delta_{\max}$. Since this would lead to a discontinuity at $\delta = 0$, it is avoided by using finite k_c.

The lines with slope k_1 and $-k_c$ define the range of possible force values, and departure from these lines takes place in the case of unloading and reloading, respectively. Between these two extremes, unloading and reloading follow the same line with slope k_2. Two possible equilibrium states are indicated as circles in figure 1, where the upper and lower circle correspond to a prestressed and stress-free state, respectively. Small perturbations lead, in general, to small deviations along the line with slope k_2, as indicated by the arrows.

A nonlinear un/reloading behaviour would be more realistic; however, due to a lack of detailed experimental information, we use the piecewise linear model as a compromise. One refinement is a k_2-value dependent on the maximum overlap that implies small and large plastic deformations for weak and strong contact forces, respectively. One model, as implemented recently [15, 23], requires an additional model parameter, $\delta^*_{\max}$, so that $k_2(\delta_{\max})$ is increasing from k_1 to k_2 (linear interpolation) with the maximum overlap, until $\delta^*_{\max}$ is reached[1]:

$$k_2(\delta_{\max}) = \begin{cases} k_2 & \text{if } \delta_{\max} \geqslant \delta^*_{\max} \\ k_{10} + (k_2 - k_{10})\delta_{\max}/\delta^*_{\max} & \text{if } \delta_{\max} < \delta^*_{\max}, \end{cases} \tag{5}$$

with the stiffness for small overlaps k_{10}, that can be chosen in the range $k_1 \leqslant k_{10} \leqslant k_2$. (For the simulations presented below, $k_{10} = k_2$ was used; a detailed parameter study is far from the scope of this paper).

While, in the case of collisions of particles with large deformations, dissipation takes place due to the hysteretic nature of the force law, stronger dissipation of small amplitude deformations is achieved by adding the viscous, velocity-dependent dissipative force from the linear contact law to the hysteretic force, such that $f^n = f^{\text{hys}} + \gamma_0 v_n$. The hysteretic model contains the linear contact model as the special case $k_1 = k_2 = k$.

2.1.3. Tangential contact model. The force in the tangential direction is implemented in the spirit of [17], where a tangential spring was introduced, in order to account for static friction. Various authors have used this idea and numerous variants were implemented; see [30] for a summary and discussion. Since we use a special implementation, which can be used for dimensions $D = 2$ and 3 alike, it is necessary to repeat the model and define the implementation. In the static case, the tangential force is coupled to the normal force via Coulomb's law, i.e. $f^t \leqslant \mu^s f^n$, where for the sliding case one has dynamic friction with $f^t = \mu^d f^n$. The dynamic and the static friction coefficients follow, in general, the relation $\mu^d \leqslant \mu^s$. However, for the following simulations we will apply $\mu = \mu^d = \mu^s$. (The first few simulations performed with $\mu^d \neq \mu^s$ do not allow for an insight into the relevance of a difference of the static and dynamic friction coefficients.) The static case requires an elastic spring, related to the tangential displacement, in order to allow for a static restoring force, i.e. a non-zero tangential force in static equilibrium due to activated Coulomb friction.

If a contact exists with non-zero normal force, the tangential force is active too, and we project the tangential spring into the actual tangential plane (this is necessary, since the frame of reference of the contact may have rotated since the last time-step for arbitrary, rotating systems, this projection requires improvement):

$$\boldsymbol{\xi} = \boldsymbol{\xi}' - \boldsymbol{n}(\boldsymbol{n} \cdot \boldsymbol{\xi}'), \tag{6}$$

where $\boldsymbol{\xi}'$ is the old spring from the last iteration, and $\boldsymbol{n}$ is the normal unit vector. This action is relevant only for an already existing spring: if the spring is new, the tangential spring length is zero anyway; however, its change/evolution is well defined below. The tangential velocity is

$$\boldsymbol{v}_t = \boldsymbol{v}_{ij} - \boldsymbol{n}(\boldsymbol{n} \cdot \boldsymbol{v}_{ij}), \tag{7}$$

with the total relative velocity

$$\boldsymbol{v}_{ij} = \boldsymbol{v}_i - \boldsymbol{v}_j + a_i \boldsymbol{n} \times \boldsymbol{\omega}_i + a_j \boldsymbol{n} \times \boldsymbol{\omega}_j, \tag{8}$$

of the surfaces of the two contacting particles. Next, we calculate the tangential test force as the sum of the tangential spring and a tangential viscous force (in analogy to the normal

[1] A limit to the slope k_2 is needed for practical reasons. If k_2 were not limited, the contact duration could become very small so that the time-step would have to be reduced below reasonable values.

viscous force)

$$\boldsymbol{f}_{\mathrm{o}}^{t} = -k_t\,\boldsymbol{\xi} - \gamma_t \boldsymbol{v}_t, \tag{9}$$

with the tangential spring stiffness k_t and a tangential dissipation parameter γ_t.

Typically, a contact starts with finite tangential velocity and $\boldsymbol{\xi} = 0$; during the first time-steps, the spring is stretched and the velocity decreases. As long as $|\boldsymbol{f}_{\mathrm{o}}^{t}| \leqslant f_C^s$, with $f_C^s = \mu^s f^n$, one has the *static friction* case (1) and, on the other hand, if $|\boldsymbol{f}_{\mathrm{o}}^{t}|$ becomes larger than f_C^s, the sliding, *dynamic friction* case (2) is active with the (possibly lower) Coulomb limit $f_C^d = \mu^d f^n$. The sliding case (2) is active as long as, in the next steps, the test force remains $|\boldsymbol{f}_{\mathrm{o}}^{t}| > f_C^d$. If the tangential force drops below the dynamic Coulomb limit, $|\boldsymbol{f}_{\mathrm{o}}^{t}| \leqslant f_C^d$, static friction becomes active again, with the (possibly larger) Coulomb limit f_C^s, giving rise to stick–slip behaviour.

In the former, *static* case (1), the tangential spring is incremented

$$\boldsymbol{\xi}' = \boldsymbol{\xi} + \boldsymbol{v}_t\,\Delta t_{\mathrm{MD}}, \tag{10}$$

with the time-step Δt_{MD} of the DEM simulation. The new value of $\boldsymbol{\xi}'$ is to be used in the next iteration in equation (6), and the tangential force $\boldsymbol{f}^t = \boldsymbol{f}_{\mathrm{o}}^{t}$ as defined in equation (9) is used. In the latter, *sliding* case (2), the tangential spring is adjusted to a length which is consistent with Coulomb's condition,

$$\boldsymbol{\xi}' = -\frac{1}{k_t}(f_C^d\,\boldsymbol{t} + \gamma_t \boldsymbol{v}_t), \tag{11}$$

with the tangential unit vector, $\boldsymbol{t} = \boldsymbol{f}_{\mathrm{o}}^{t}/|\boldsymbol{f}_{\mathrm{o}}^{t}|$, defined by the direction of the force in equation (9), and thus the magnitude of the Coulomb limit is used. Inserting $\boldsymbol{\xi}'$ into equation (9) leads to $\boldsymbol{f}_{\mathrm{o}}^{t} \approx f_C^d \boldsymbol{t}$. Note that $\boldsymbol{f}_{\mathrm{o}}^{t}$ and $\boldsymbol{v}_t$ are not necessarily parallel in three dimensions. However, the mapping in equation (11) works always, rotating the new spring such that the direction of the frictional force is unchanged and, at the same time, limiting the spring in length according to Coulomb's law. In short notation the tangential force on particle i reads

$$\boldsymbol{f}_i^t = +\min\left(f_C, |\boldsymbol{f}_{\mathrm{o}}^{t}|\right)\boldsymbol{t}, \tag{12}$$

where f_C follows the selection rules described above.

Note that the tangential force described above is identical to the classical Cundall–Strack spring only in the limits $\mu = \mu^s = \mu^d$ and $\gamma_t = 0$. The sequence of computations and the definitions and mappings into the tangential direction, however, is new to our knowledge insofar as it accounts for different static and dynamic friction coefficients and can be easily generalized to three dimensions.

2.1.4. Background friction. Note that the viscous dissipation takes place in a two-particle contact. In the bulk material, where many particles are in contact with each other, dissipation can be very inefficient due to long-wavelength cooperative modes of motion [31, 32]. Therefore, an artificial background is introduced, so that the total force on particle i is

$$\boldsymbol{f}_i = \sum_{\mathrm{c}} \left(f_i^n \hat{\boldsymbol{n}} + \boldsymbol{f}_i^t\right) - \gamma_{\mathrm{b}} \boldsymbol{v}_i, \tag{13}$$

with a viscous background damping constant γ_{b} for a rapid equilibration.

2.1.5. Other forces. Forces other than those mentioned above, such as long-range forces (electrostatic or van der Waals), contact couples, rolling or torsion friction, are neglected in this study as well as a possible non-spherical shape of the particles. Research in this direction is in progress, however.

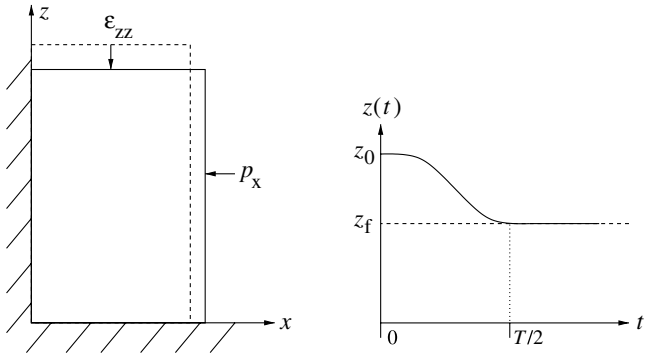

Figure 2. Left: schematic drawing of the model system. Right: position of the top wall as function of time (with deformation time $t_s = T/2$) for the strain-controlled wall motion with cosine period T.

2.2. Model system

The 'experiment' chosen is the biaxial box set-up, see figure 2, where the left and bottom walls are fixed. The right wall is subject to a constant stress, and the top wall follows a predefined strain path [10, 14]. In a typical 'experiment', the top wall is smoothly and slowly shifted downward (according to a half cosine function), in order to avoid shocks and inertia effects, respectively. The right wall has a mass, m_w, and its motion is stress controlled, dependent on the force $F(t)$ exerted on it by the material in the box and by a dashpot that damps its motion.

2.3. Parameters

The system examined in the following contains $N = 1950$ particles with radii a_i randomly drawn from a homogeneous distribution between $a_{\min} = 0.5\times10^{-3}$ m and $a_{\max} = 1.5\times10^{-3}$ m. The masses of the cylindrical particles with height $h = 2.0 \times 10^{-4}$ m are $m_i = \rho\pi h a_i^2$, with the density $\rho = 2.0 \times 10^3$ kg m^{-3}. The total mass of the particles in the system is thus $M \approx 0.0026$ kg, with the typical reduced mass of a pair of particles with mean radius $m_{12} \approx 0.67 \times 10^{-6}$ kg. The wall properties are $m_w = 10^{-4}$ kg and $\gamma_w = 2$ kg s^{-1}. If not explicitly mentioned, the material parameters are $k_1 = k_2/2$, $k_2 = 10^5$ N m^{-1}, $\gamma_0 = \gamma_t = 0.02$ kg s^{-1}, and $\gamma_b = 10^{-5}$ kg s^{-1}, $\mu = 0.5$, and $k_t/k = 0.2$. This leads to a typical contact duration $t_c = 0.82 \times 10^{-5}$ s and a restitution coefficient of $r = 0.89$, with the integration time-step used, $\Delta t_{MD} = 0.2 \times 10^{-6}$ s. The choice of parameters is rather arbitrary (with respect to the linear force model with the rather small stiffness); however, the finding below that the stiffness tensor scales with the spring constant rectifies it *a posteriori*, i.e. the results do not depend on the stiffness explicitly. Additional simulations (not shown here) also confirm this statement. Note that the choice of the stiffness and a possible nonlinear force law is more important for dynamic systems, for sound propagation for example, than for the quasi-static system presented here.

2.4. Initial configuration

Initially, the particles are randomly distributed in a huge box, with rather low overall density, and friction as well as cohesion is switched off. Then the box is compressed with isotropic pressure $p = p_x = p_z$, in order to achieve an initial condition that is as isotropic as feasible; there is remaining anisotropy of the order of a few per cent in some situations, however. The

configuration is relaxed until the kinetic energy is several orders of magnitude smaller than the potential contact energy. Starting from this relaxed, over-consolidated, isotropic initial configuration, the strain is applied to the top wall and the response of the system is examined with friction and cohesion active.

3. Averaging and micro–macro transition

In order to obtain macroscopic quantities, averages are taken over single-contact elementary tensors, as derived in [14]. Note that we focus here on those quantities that can be obtained from static snapshots and do not rely on (real) displacements; see [14, 15, 33] for more details. The simplest averaging approach is used here, i.e. a contact is taken into account if the corresponding particle centre lies within the averaging volume (alternatives are discussed in [14]). This corresponds to a pre-averaging over single particles and then subsequent averaging over the particles with volume V^{p} in the volume. Cast into an equation this reads

$$Q = \langle Q \rangle = \frac{1}{V} \sum_{p \in V} V^{\mathrm{p}} Q^{\mathrm{p}}, \tag{14}$$

where Q is the averaged macroscopic quantity and $Q^{\mathrm{p}} = (1/V^{\mathrm{p}}) \sum_{c=1}^{C^{\mathrm{p}}} V_{\mathrm{c}} Q^c$ is the pre-averaged particle quantity with the contact quantity Q^c and the volume associated to the contact, V_{c}. Here, the subscript $p \in V$ denotes the particle-in-volume averaging procedure. The simplest macroscopic quantity is the volume fraction ν, as obtained from $Q^{\mathrm{p}} = 1$.

3.1. The fabric tensor

For one particle with C^{p} contacts, the fabric tensor is defined as the sum, over all contacts, of the dyadic product formed by the normal vectors:

$$F^{\mathrm{p}}_{\alpha\beta} = \sum_{c=1}^{C^{\mathrm{p}}} n_\alpha n_\beta, \tag{15}$$

with the trace $\mathrm{tr}\boldsymbol{F}^{\mathrm{p}} = F^{\mathrm{p}}_{\gamma\gamma} = C^{\mathrm{p}}$. Greek subscripts identify the tensor elements and summation over equal indices is implied. In a large volume, with some distribution of particle radii, the relation between trace of fabric, density and average contact number C is, according to [34], $F_{\alpha\alpha} = g_2 \nu C$, with the average fabric, i.e. a contact number density,

$$F_{\alpha\beta} = \frac{1}{V} \sum_{p \in V} V^{\mathrm{p}} \sum_{c=1}^{C^{\mathrm{p}}} n_\alpha n_\beta, \tag{16}$$

and the correction factor

$$g_2 \approx 1 + \frac{\sqrt{3}}{\pi} \left(\frac{\overline{a^3}}{\overline{a}\,\overline{a^2}} - 1 \right), \tag{17}$$

dependent on the first three moments of the size distribution $\overline{a^k}$ (with $k = 1, 2, 3$). In brief, g_2 corrects for the fact that the coordination number of different sized particles depends on their surface area, so that a monodisperse packing has $g_2 = 1$, whereas a polydisperse packing has $g_2 > 1$ with magnitude increasing with the width of the size distribution. Thus, a polydisperse packing has a higher contact number density than a monodisperse system of comparable density. It was shown recently that the correction, as tested for frictionless systems [34], is also relevant for frictional packings [14, 15].

3.2. The stress tensor

In the averaging volume V, one obtains the approximate (averaged) macroscopic stress from the dyadic product of the contact force, $\boldsymbol{f}^c$, and the (particle-centre to contact) branch vector, $\boldsymbol{l}^c$,

$$\sigma_{\alpha\beta} = \frac{1}{V}\sum_{p\in V}\sum_{c=1}^{C^{\rm p}} l^c_\alpha f^c_\beta. \tag{18}$$

Note that the particle volume in equation (14) cancels due to the volume weight. Regarding the units, we interpret the stress as a potential energy density, with all contacts within V contributing. This is equivalent to the traditional definition of stress being the force per area on the surface of V.

3.3. The elastic stiffness tensor

The stiffness tensor relates the change of stress to an applied strain. For particles with branch vector length $l = l^c$, and identical spring constants $k = k^c$, and $k^t = (k^t)^c$, one has:

$$C_{\alpha\beta\gamma\phi} = \frac{1}{V}\sum_{p\in V}\left(k\sum_{c=1}^{C}(2l^2)n^c_\alpha n^c_\beta n^c_\gamma n^c_\phi + k^t\sum_{c=1}^{C}(2l^2)n^c_\alpha t^c_\beta n^c_\gamma t^c_\phi\right), \tag{19}$$

where the two contributions from normal and tangential springs can be examined separately. Note that this result can already be found in the literature [14, 35, 36] in similar form; however, we provide it here again, for the sake of completeness.

4. Averaged quantities from simulations

As the essential step of a micro–macro transition, in the following, simulation results are presented for various side pressures p, different cohesion strength, $k_{\rm c}$, and different friction coefficients, μ. Averages are performed such that parts of the system close to the walls are disregarded in order to avoid boundary effects. This means that the averaging volume is about 64% of the total volume. A particle contact is taken into account for the average if the corresponding particle-centre lies within the averaging volume V.

4.1. Density dependence on isotropic confining pressure

The first quantity of interest is the density (volume fraction), ν, as function of the side pressure p. After the preparation procedure (with $\mu = 0$ and $k_{\rm c} = 0$), before deformation, the initial density and the pressure follow the relation

$$\frac{p}{p_0} = (\nu - \nu_0)^\alpha, \tag{20}$$

with $\alpha \approx 4/3$, $\nu_0 = 0.8361 \pm 0.0005$, and $p_0/k_2 = 1.16 \pm 0.05$. (Note that pressure p here is actually the product of the actual pressure and h, the height of the particles, and thus has units N m^{-1}. Throughout the rest of the paper, pressure will be provided dimensionless, in units of $10^{-5}\,k_2$.) This is obtained if the whole box with all particles is taken into account and the pressure is measured at the walls (normal wall force divided by wall area). If only the central volume is taken into account, without the particles close to the wall, the relation is well fitted by the same curve with $\nu_0 = 0.848 \pm 0.002$, i.e. with a higher critical density ν_0, because the density in the bulk is somewhat higher, and a slightly smaller exponent results. In the limit $p \to 0$, the critical density ν_0 corresponds to the maximal packing density for rigid,

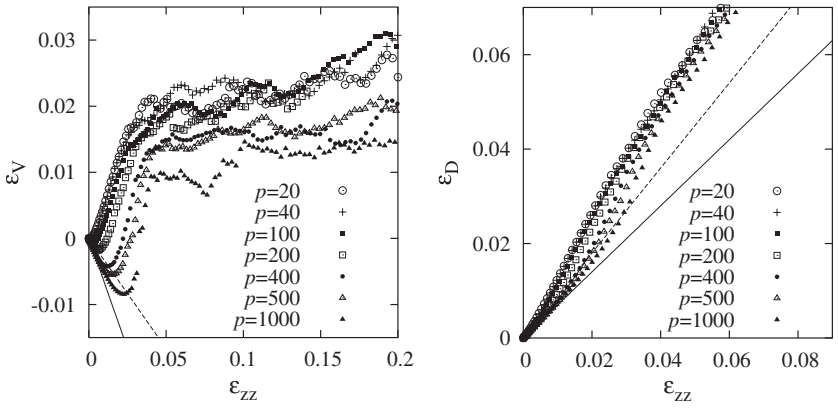

Figure 3. Left: volumetric strain, ε_V, (negative values mean compression) plotted against the vertical strain ε_{zz}. The dashed and solid lines correspond to $m_V\varepsilon_{zz}$, with $m_V = -0.2$ and -0.6, respectively. Right: deviatoric strain, ε_D, plotted against ε_{zz}, with the lines corresponding to $(1 + m_V/2)\varepsilon_{zz}$.

frictionless and cohesionless particles [37], and to the minimal density for which a stable, static packing is possible. Note, however, that changing either the preparation procedure, the size distribution function, the friction coefficient or the cohesion, will affect the value of ν_0.

4.2. Isotropic and deviatoric deformation

During the deformation as controlled by the top wall, we report the volumetric strain, $2\varepsilon_V = \Delta V/V$, and the deviatoric strain $\varepsilon_D = (\varepsilon_{zz} - \varepsilon_{xx})/2$, with the vertical and horizontal strains, $\varepsilon_{zz} = 1 - z/z_0$, and $\varepsilon_{xx} = 1 - x/x_0$. Initially, one has $\varepsilon_V \approx -(\varepsilon_{zz} + \varepsilon_{xx})/2 \approx m_V\,\varepsilon_{zz}$, and the system is compressed, $\varepsilon_V < 0$, which is more pronounced for larger side pressures; see figure 3. From the initial slope m_V, one can obtain a Poisson ratio, $\nu_P = -\varepsilon_{xx}/\varepsilon_{zz} = 1 + m_V$, in the range $0.4 \leqslant \nu_P \leqslant 0.8$, decreasing with increasing pressure. The initial compression regime is followed by dilation (which sets in later for higher pressures), until a quasi-steady-state critical flow regime is reached, where the density is almost constant besides a weak tendency towards further dilation. The level of saturation decreases with increasing side pressure or, in other words, the critical state density increases with increasing side pressure.

The deviatoric strain, ε_D, quantifies the amount of shear the medium undergoes in addition to, and independently of, the compression/dilatancy. Initially, one has $\varepsilon_D \approx (1 + 2/m_V)\varepsilon_V$; the deviation from this asymptotic regime begins earlier for smaller side pressure. For larger deformations, the deviatoric strain becomes almost pressure independent, i.e. in the critical state flow regime, $\varepsilon_V \approx$ constant, the system undergoes only deviatoric strain.

An initially dilute granular medium (weak confining pressure) thus shows dilation almost from the beginning, whereas a denser granular material (under stronger confining pressure) can be compressed even further by the relatively strong external forces, before dilation starts. The range of density changes is 0.02–0.03 in volume fraction, or volumetric stain, for the parameters used here. The material undergoes—due to the boundary conditions chosen—compression, dilation and volume-conserving critical state flow. In addition, the system undergoes continuous shear, where the shear deformation is stronger, and grows more quickly for smaller confining stress p; i.e. for larger p, the material is more resistant to shear.

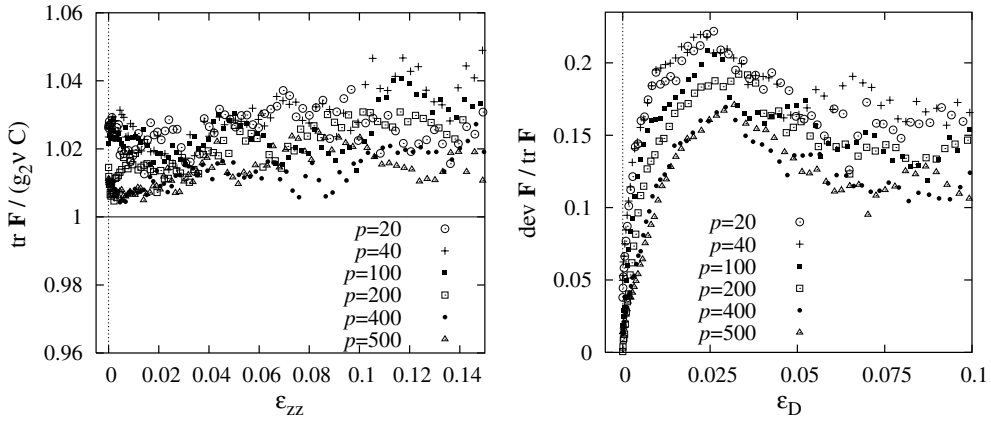

Figure 4. Left: quality factor for the trace of the fabric tensor scaled by the analytical prediction $g_2\nu C$ from [34], for different pressures p, as a function of the vertical deformation. Right: deviatoric fraction of the fabric tensor from the same simulations plotted against the deviatoric strain.

4.3. Fabric tensor

The fabric tensor is computed according to equation (16), and its isotropic and deviatoric contributions are displayed in figure 4. The isotropic contribution (the contact number density) is scaled by the prediction from [34], see equation (17), and the deviation from the prediction is between 1% and 3%, where the larger side pressure data are in better agreement (smaller deviation). Note that the correction due to the factor g_2 corresponds to about 9%, and that the data are taken in the presence of friction, in contrast to the simulations by [34], a source of discrepancy which accounts, in our opinion, for the remaining deviation.

The anisotropy of the granular packing is quantified by the deviatoric fabric, as displayed in its scaled form in figure 4. The anisotropy is initially of the order of a few per cent at most: thus the initial configurations are not perfectly isotropic. With increasing deviatoric deformation, the anisotropy grows, reaches a maximum and then saturates on a lower level in the critical state flow regime. The scaled fabric grows faster for smaller side pressure and is also relatively larger for smaller p. The non-scaled fabric deviator, astonishingly, grows to values around $f_{\rm D}^{\rm max}\,{\rm tr}\,\boldsymbol{F} \approx 0.56 \pm 0.03$, independently of the side pressures used here (data not shown; see [14, 15] for details). Using the definition $f_{\rm D} := {\rm dev}\boldsymbol{F}/{\rm tr}\boldsymbol{F}$, the functional behaviour,

$$\frac{\partial f_{\rm D}}{\partial \varepsilon_{\rm D}} = \beta_f \left(f_{\rm D}^{\rm max} - f_{\rm D}\right), \tag{21}$$

was evidenced from simulations in [14], with $f_{\rm D}^{\rm max}\,{\rm tr}\,\boldsymbol{F} \approx$ constant, and the deviatoric rate of approach $\beta_f = \beta_f(p)$, decreasing with increasing side pressure. The differential equation is solved by an exponential function that describes the approach of the anisotropy $f_{\rm D}$ to its maximal value, $1 - (f_{\rm D}/f_{\rm D}^{\rm max}) = \exp\left(-\beta_f \varepsilon_{\rm D}\right)$, but not beyond.

4.4. Stress tensor

The behaviour of the stress is displayed in figure 5, where the isotropic stress $(1/2){\rm tr}\,\boldsymbol{\sigma}$ is plotted in units of p, and the deviatoric fraction is plotted in units of the isotropic stress. Note that the tangential forces do not contribute to the isotropic stress here since the corresponding

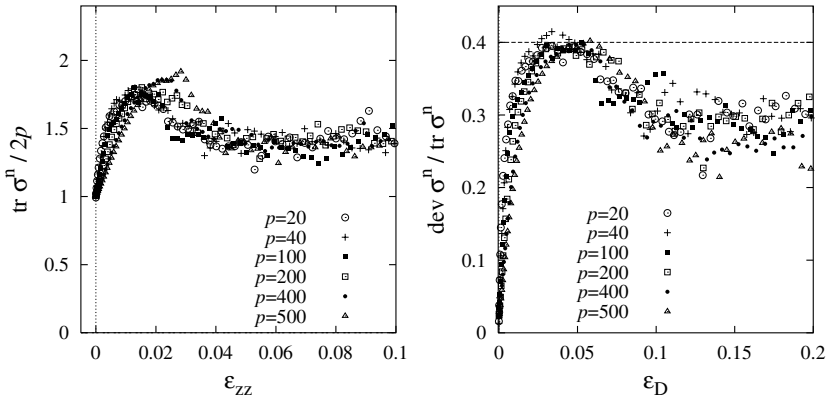

Figure 5. Non-dimensional stress tensor contributions for different p. The isotropic (left) and the deviatoric fractions (right) are displayed as functions of the vertical and deviatoric strain, respectively.

entries in the averaging procedure compensate. From figure 5, we evidence that both normal contributions, the non-dimensional trace and the non-dimensional deviator, behave similarly, independent of the side pressure: starting from an initial value, a maximum is approached, where the maximum is only weakly dependent on p.

The increase of stress is faster for lower p. After the maximum is reached, the stresses decay and approach a smaller value in the critical state flow regime. Using the definitions $s_{\mathrm{V}} := \mathrm{tr}\,\boldsymbol{\sigma}/(2p) - 1$ and $s_{\mathrm{D}} := \mathrm{dev}\boldsymbol{\sigma}/\mathrm{tr}\boldsymbol{\sigma}$, the maximal (non-dimensional) isotropic and deviatoric stresses are $s_{\mathrm{V}}^{\max} \approx 0.8 \pm 0.1$ and $s_{\mathrm{D}}^{\max} \approx 0.4 \pm 0.02$, respectively, with a rather large error margin. The corresponding values at critical state flow are $s_{\mathrm{V}}^{c} \approx 0.4 \pm 0.1$ and $s_{\mathrm{D}}^{c} \approx 0.29 \pm 0.04$.

The evolution of the *deviatoric stress* fraction, s_{D}, as a function of ε_{D}, is displayed in figure 5. Like the fabric, the deviatoric stress also exponentially approaches its maximum. This is described by the differential equation

$$\frac{\partial s_{\mathrm{D}}}{\partial \varepsilon_{\mathrm{D}}} = \beta_s \left(s_{\mathrm{D}}^{\max} - s_{\mathrm{D}}\right), \tag{22}$$

where $\beta_s = \beta_s(p)$ is decaying with increasing p (roughly as $\beta_s \approx p^{-1/2}$). For more details on the deviatoric stress and also on the tangential contribution to the stress, see [14, 15].

4.5. Stiffness tensor

Given an arbitrary (small) deformation, the stiffness tensor relates the stress changes to the deformation

$$\delta\sigma_{\alpha\beta} = C_{\alpha\beta\gamma\phi}\varepsilon_{\gamma\phi} + \delta\sigma_{\alpha\beta}^{\mathrm{struct.}}, \tag{23}$$

where the first term corresponds to the elastic (reversible) structural anisotropy, and the second term contains the stress changes due to a change in structure. The stiffness tensor entries $C_{\alpha\beta\gamma\phi}$ were discussed in detail in [14, 15], where it was concluded that there are typically only three different moduli, $C_1 := C_{xxxx}$, $G := C_{xxzz} = C_{zzxx}$, and $C_2 := C_{zzzz}$, due to normal forces, in the coordinate system of the biaxial box. Tensor entries with an odd number of indices are practically zero. Also the stiffness entries due to the tangential forces are related to these three moduli [14], but will not be discussed in detail here.

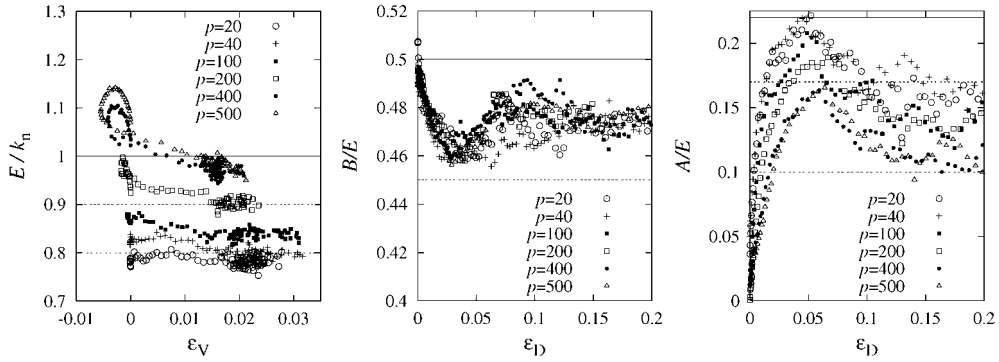

Figure 6. Left: isotropic modulus E, scaled by k_n, plotted as a function of ε_{V}; middle: shear modulus ratio, B/E, plotted as a function of ε_{D}; and right: anisotropic modulus ratio, A/E, plotted as a function of ε_{D}.

In the following, we recall [14, 15], and rewrite equation (23) in terms of $\delta\sigma_{\mathrm{V}}$, $\delta\sigma_{\mathrm{D}}$, ϵ_{V}, and ε_{D}, where the indices V and D denote the isotropic and the deviatoric contributions, respectively. Note that $\epsilon_{\mathrm{V}} = -\varepsilon_{\mathrm{V}}/2$ is used here for convenience. Since, in the biaxial box system, the eigensystem of the tensors is oriented according to the wall geometry, a scalar formulation is possible for the isotropic stress:

$$\delta\sigma_{\mathrm{V}} = \delta\sigma_{\alpha\alpha}/2 = E\left(\epsilon_{\mathrm{V}} + \frac{A}{E}\varepsilon_{\mathrm{D}}\right) + \delta\sigma_{\alpha\alpha}^{\mathrm{struct.}}/2, \tag{24}$$

with $\epsilon_{\mathrm{V}} = -(1/2)(\varepsilon_{xx} + \varepsilon_{zz})$, $\varepsilon_{\mathrm{D}} = (1/2)(\varepsilon_{zz} - \varepsilon_{xx})$, and the isotropic compression modulus $E = (C_1 + C_2 + 2G)/2$ that relates an isotropic deformation to an isotropic stress change, and the anisotropic modulus $A = (C_2 - C_1)/2$ that relates isotropic (deviatoric) deformations, to deviatoric (isotropic) stress changes. For the deviatoric stress one has

$$\delta\sigma_{\mathrm{D}} = \delta\left(\sigma_{zz} - \sigma_{xx}\right)/2 = E\left(\frac{A}{E}\epsilon_{\mathrm{V}} + \frac{B}{E}\varepsilon_{\mathrm{D}}\right) + \delta\sigma_{\mathrm{D}}^{\mathrm{struct.}},$$

with the deviatoric shear modulus $B = (C_1 + C_2 - 2G)/2 = E - 2G$ that relates an anisotropic deformation to an anisotropic stress change. Thus the anisotropic, elastic material behaviour is described (in biaxial Cartesian coordinates) by the compression modulus E and the two dimensionless numbers A/E and B/E, which quantify anisotropy and deviatoric shear strength, respectively.

From the simulations presented in the previous subsections, the moduli are plotted in figure 6. We observe first that the modulus E is proportional to the trace of the fabric tensor, $E \propto \mathrm{tr}\,\boldsymbol{F}$ (data not shown). From the plot against the volumetric deformation, we observe that E increases with pressure from about $0.78k_n$ to $1.05k_n$, both in the initial state and the critical flow state. The initial compression leads to a temporary increase of stiffness in the range from 1% to 10%, an effect which is more pronounced for larger confining pressure.

The shear stiffness ratio B/E starts at a value close to 0.5 and rapidly drops by 6–8%, then increases a few per cent and levels out at values around 0.475 ± 0.010 in the critical state regime.

The anisotropic stiffness ration A/E increases from zero to peak values from 0.16 to 0.22, for small deviatoric strain, like the deviatoric fraction of the fabric tensor. After the peak, A/E decays and reaches values between 0.1 and 0.17. The anisotropic modulus A/E, related to the isotropic modulus, becomes somewhat less important with increasing confining pressure.

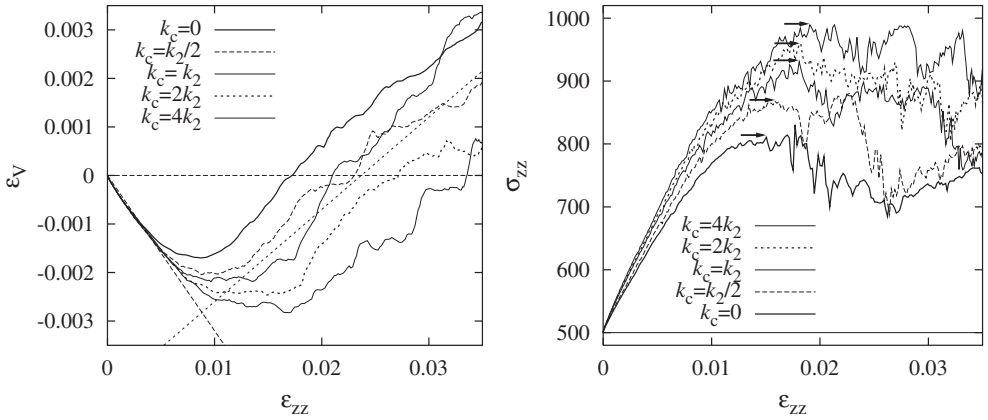

Figure 7. Simulation results from runs with $k_1 = k_2/2$, and different cohesion strength k_c, as given in the inset for $p = 500$. Left: the volume change is plotted against ε_{zz}, and the straight lines indicate the slopes −0.32 and +0.19. Right: vertical stress σ_{zz} plotted against ε_{zz}; the arrows indicate the peak stress.

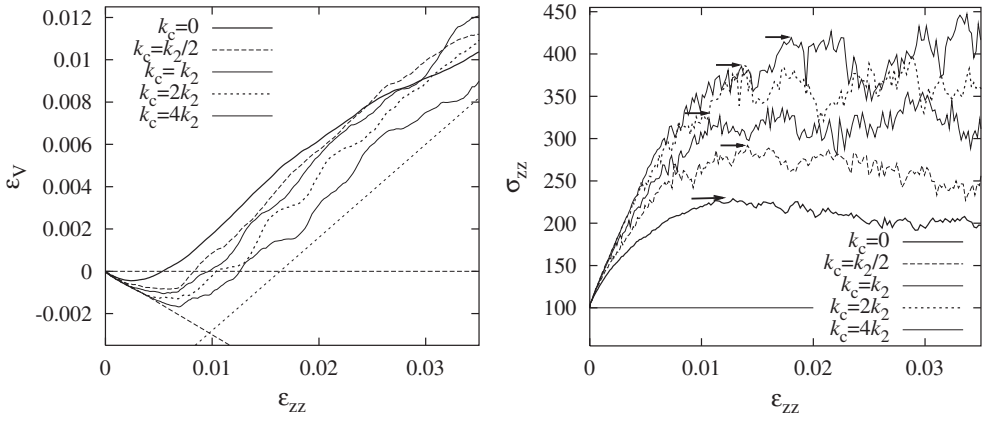

Figure 8. The same as in figure 7, only here $p = 100$, and the straight lines indicate the slopes −0.30 and +0.44.

4.6. Variation of the microscopic cohesion

Two series of simulations with varying cohesion strength, k_c, and vanishing friction, $\mu = 0$, are performed at initial confining pressures $p = 500$ and 100; see figures 7 and 8. For small strain ε_{zz}, the material is compressed, as indicated by negative ε_V, extending to larger (negative) values for stronger cohesion k_c and larger external pressure p. The initial slope, $m_V \approx -0.31$, can be related to the Poisson ratio $\nu_P = 1 + m_V \approx 0.69$, and appears to be independent of both cohesion strength and pressure, in the absence of friction.

When the upper wall continues to move, dilatancy is evidenced at ε_{zz}-values between 1% and 2% for large external stress, but already for much smaller strain if the external pressure is smaller. The positive slope can be related to a dilatancy angle [10, 38], as used in some material models. The onset of dilatancy typically takes place before the maximum vertical stress is achieved, and thus before the failure of the material. The transition from the compressive to the dilatant regime is delayed to larger strain by stronger cohesion and stronger external pressure.

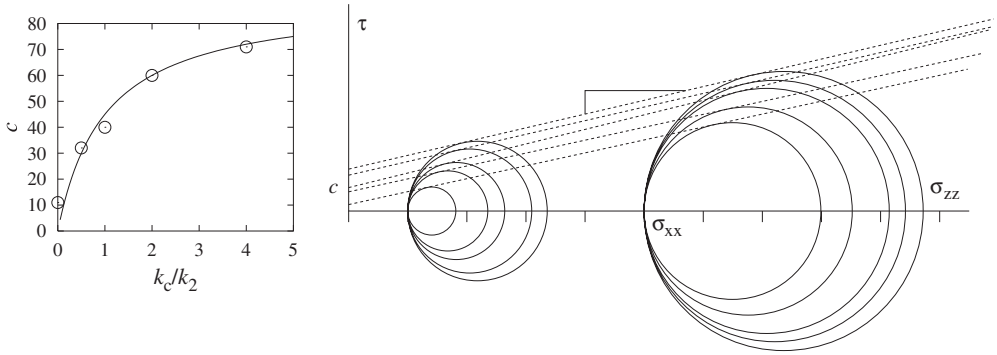

Figure 9. Yield surface for simulations with $\mu = 0$ and varying k_c. Left: macroscopic cohesion c as function of the cohesion strength k_c, with the maximum attractive force $c \propto (k_2 - k_1)/(k_2 + k_c)$ given as solid curve. Right: Mohr circles at failure, for the simulations in figures 7 and 8. The left end of the circle corresponds to the fixed pressure p, the right end to the vertical pressure σ_{zz} at failure. The angle indicates a slope of about 0.23.

From the initial slope of the stress–strain curves, one could extract a modulus of the material, increasing with increasing strength of cohesion. After failure (see the figures), softening is obtained for large p and weak cohesion. The critical-state regime is here also accompanied by strong fluctuations. The maximum stress from each simulation is indicated by an arrow in the figures. For more details concerning the rate dependence and the relaxation rates of these simulations, see [10].

4.7. Yield stress and macroscopic cohesion

The yield stresses from figures 7 and 8 are combined in figure 9 as Mohr circles. Each set of Mohr circles corresponds to a fixed external pressure p, and different circles correspond to different $k_c/k_2 = 0$, 1/2, 1, 2, and 4, from the smallest to the largest circle, respectively. The tangent to a pair of circles with the same cohesion strength is plotted as a dotted line for all pairs. The slope of the lines is $\tan\phi \approx 0.23$, corresponding to an internal friction angle $\phi \approx 13°$. Due to the absence of any microscopic friction in the model, the macroscopic friction, $\tan\phi$, has to be caused by the geometry of the packing, which causes a shear resistance due to interlocked particles.

The macroscopic *cohesion*, c, of the material can be obtained as the point of intersection of the dashed line and the zero vertical axis, as detailed in [10]; see figure 9. We note that c is not linear in k_c, but saturates after a strong increase. The solid curve gives the maximal attractive force, $f_{\min}$, see section 2.1.2, which behaves analogously, thus relating the macroscopic cohesion, c, to the microscopic attractive force, as defined in the contact model.

4.8. Variation of the friction coefficient

In the final set of simulations, we restrict ourselves to cohesionless material, $k_c = 0$, but here the microscopic coefficient of friction μ is varied. In figure 10, volumetric strain and deviatoric stress are plotted for simulations with $p = 200$ and different μ.

The volumetric strain shows compression (decrease), dilatancy (increase) and critical state behaviour (constant), like in the figures above. Here we note that the rate and the amount of dilatancy increases strongly with increasing μ, from very small values for $\mu = 0$ up to volume changes of around 2% for $\mu = 0.5$. The deviatoric stress increases, then the slope gradually

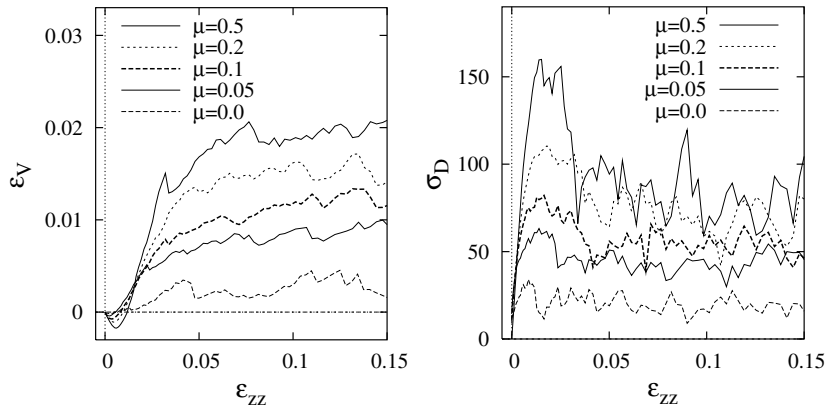

Figure 10. Left: volumetric strain as function of vertical strain from simulations with $p = 200$ and different coefficients μ. Right: anisotropic stress as function of vertical strain from the same simulations.

decreases (softening), until the stress reaches its maximum (peak yield stress). After the peak, further softening/weakening behaviour (with negative slope) is followed by a constant, strongly fluctuating stress for larger deformations, in the critical state flow regime. Peak stress, critical state stress and also the magnitude of softening increase with increasing μ.

For $\mu = 0.5$, somewhat softer particles, and larger viscosity, we show in figure 11 (left) that the yield surface is approximately linear with a slope of 0.588. Given this linearity together with the linearity for $\mu = 0$, one can extract the macroscopic friction coefficients, $\tan\phi$, from the peak stresses of a single simulation, as shown in figure 10, using the relation

$$\sin\phi = \frac{\sigma_{zz} - \sigma_{xx}}{\sigma_{zz} + \sigma_{xx}}. \tag{25}$$

Data for different simulations with different initial conditions and different deformation times t_s are shown in figure 11 (right). Macroscopic friction is evidenced already for vanishing microscopic friction. For larger μ-values, the macroscopic friction bends and seems to saturate. Simulations with comparatively large viscosity and faster compression lead to larger friction. Thus it is important to deform the sample very slowly in order to obtain quasi-static results. Also the initial condition affects the result, i.e. simulations prepared with strong friction, when compressed with smaller friction, first collapse and later lead to slightly larger peak friction.

4.9. Summary of macroscopic material parameters

From the simulation data, it is possible to obtain the following material parameters, as based on an isotropy/homogeneity assumption:

(i) The initial slope of the volumetric strain allows one to determine the Poisson ratio, dependent on the side stress p and microscopic friction μ, but almost independent of cohesion strength k_c.

(ii) The slope of the volumetric strain in the dilatancy regime (about +0.4 without friction and $p = 100$, about +0.2 without friction and $p = 500$, and up to about +0.8 with strong friction, but without cohesion) is related to the dilatancy angle. Dilatancy is hindered by large side stresses, but much stronger dilatancy is evidenced in the presence of strong friction. Cohesion seemingly does not affect the dilatancy.

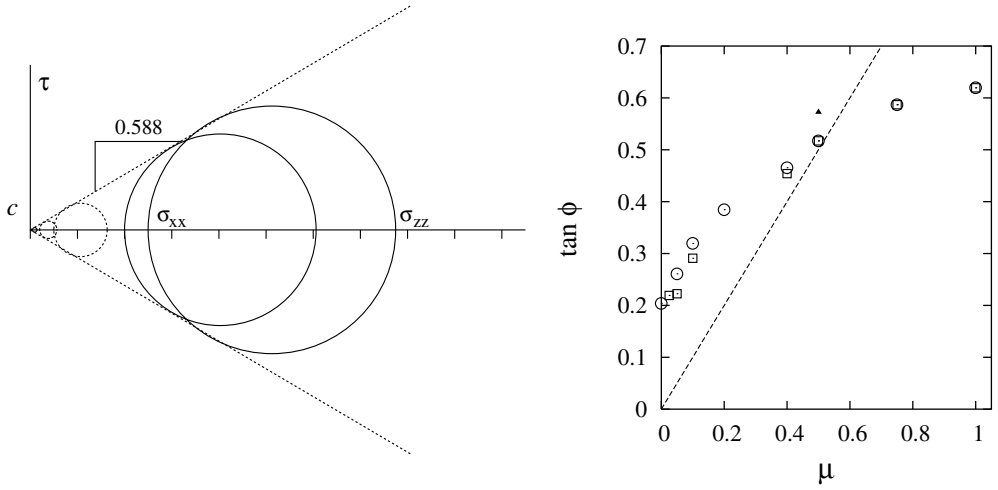

Figure 11. Left: Mohr circle representation of the flow function at peak stress from simulations with different pressure and $\mu = 0.5$, and fast deformation, $t_s \approx 0.5$ s. Right: macroscopic friction coefficient as a function of the microscopic friction for fast (solid triangles) and slow deformation $t_s \approx 10$ s (open symbols). Simulations were started from a configuration prepared with $\mu = 0$ (squares) and with $\mu = 0.5$ (circles).

(iii) The initial slope of the pressure, when plotted against the volumetric strain, is related to the macroscopic bulk modulus E, which like the shear and the anisotropic moduli, B and A, can also be obtained from the stiffness tensor. The shear modulus is almost constant, $B \approx E/2$, for the boundary conditions used here, while the anisotropic modulus (identical to the deviatoric fabric fraction) increases from zero to a maximal value, and shows softening and critical state flow behaviour for larger deformations.

(iv) The peak (yield) stress is related to the flow function of the material. Also, in the absence of microscopic friction, there is a macroscopic friction due to geometrical, structural effects. With increasing microscopic friction, the macroscopic friction also increases, until it tends to saturate for values $\mu > 1$. We remark that these results are sensitive to details of sample preparation and parameter choice.

As a final remark, we note that some of the micro–macro transition results depend slightly on the averaging procedure and averaging volume.

5. Summary and conclusion

In summary, a set of DEM simulations was presented, and several macroscopic material parameters, such as the macroscopic cohesion, the friction angle, and three bulk moduli, were extracted from the simulation data with cohesion (no friction) and with friction (no cohesion), for different confining pressures. The macroscopic cohesion could be related to the minimal force (the maximal attractive force) in the microscopic contact model. The macroscopic friction angle is not directly related to the microscopic friction angle, due to geometrical interlocking and dilatancy effects; furthermore, the macroscopic friction seems to saturate for large microscopic friction coefficients.

From the presented data, it can be concluded that there are basically only three different quantities in the stiffness tensor (scaling with the microscopic spring stiffness used for the simulation), which quantify the stress response of a static granular packing, disregarding

changes of the structure. The bulk modulus E slightly increases with density and confining pressure. The shear modulus B is almost invariant relative to E, and the anisotropic modulus A shows the largest variation from the initial isotropic state to peak stress, and then decays to the critical state flow value. The magnitude of the maximum of A/E is inversely proportional to the confining pressure.

Stress responses are proportional to the isotropic fabric F_V in magnitude, because this is proportional to the isotropic modulus E. The deviatoric fraction of the fabric behaves like the anisotropic modulus A/E. For both deviator fabric and stress, an exponential approach to the maximal value was observed, with rate of approach increasing with decreasing confining stress.

Together with shear band localization, the role of particle rotations is also an open issue, as related to micro-polar constitutive models: in both simulation and experiment, rotations are active in the shear band. Local averaging in smaller averaging volumes (areas), the corresponding parameter identification, and the micro–macro transition for anisotropic micro-polar continuum models is a challenge for the future, like the implementation and simulation of experimentally determined force laws in more realistic three-dimensional systems.

Acknowledgments

We thank E Clément, J Jenkins, N P Kruyt, M Madadi, F Nicot, R G Rojo, C Thornton, J Tomas, and R Tykhoniuk for helpful discussions and acknowledge the support of the Deutsche Forschungsgemeinschaft (DFG). This work is part of the research programme of the Stichting voor Fundamenteel Onderzoek der Materie (FOM), financially supported by the Nederlandse Organisatie voor Wetenschappelijk Onderzoek (NWO) and the Stichting Shell Research.

References

[1] Herrmann H J, Hovi J-P and Luding S (ed) 1998 *Physics of Dry Granular Media* (*NATO ASI Series E 350*) (Dordrecht: Kluwer)
[2] Vermeer P A, Diebels S, Ehlers W, Herrmann H J, Luding S and Ramm E (ed) 2001 *Continuous and Discontinuous Modelling of Cohesive Frictional Materials* (*Springer Lecture Notes in Physics* vol 568) (Berlin: Springer)
[3] Kishino Y (ed) 2001 *Powders & Grains 2001* (Rotterdam: Balkema)
[4] Chang C S and Ma L 1991 A micromechanical-based micropolar theory for deformation of granular solids *Int. J. Solids Struct.* **21** 67–86
[5] Babić M 1997 Average balance equations for granular materials *Int. J. Eng. Sci.* **35** 523–48
[6] Bagi K 1999 Microstructural stress tensor of granular assemblies with volume forces *J. Appl. Mech.* **66** 934–6
[7] Oda M and Iwashita K 2000 Study on couple stress and shear band development in granular media based on numerical simulation analyses *Int. J. Eng. Sci.* **38** 1713–40
[8] Bardet J P and Vardoulakis I 2001 The asymmetry of stress in granular media *Int. J. Solids Struct.* **38** 353–7
[9] Suiker A S J, Metrikine A V and de Borst R 2001 Comparisons of wave propagation characteristics of the cosserat continuum model and corresponding discrete lattice models *Int. J. Solids Struct.* **38** 1563–83
[10] Luding S and Herrmann H J 2001 Micro–macro transition for cohesive granular media *Bericht Nr. II-7* ed S Diebels (Universität Stuttgart: Inst. für Mechanik)
[11] Peters J P and Horner D A 2002 Errors of scale in discrete element computations *Discrete Element Methods: Numerical Modeling of Discontinua (Santa Fe, 2002. ASCE)* ed In K Cook and R P Jensen pp 56–67
[12] Goldhirsch I and Goldenberg C 2002 On the microscopic foundations of elasticity *Eur. Phys. J.* E **9** 245–51
[13] Kruyt N P 2003 Statics and kinematics of discrete cosserat-type granular materials *Int. J. Solids Struct.* **40** 511–34
[14] Luding S 2004 Micro–macro transition for anisotropic, frictional granular packings *Int. J. Solids Struct.* **41** 5821–36
[15] Luding S 2004 Micro–macro models for anisotropic granular media *Modelling of Cohesive-Frictional Materials* ed P A Vermeer, W Ehlers, H J Herrmann and E Ramm (Leiden: Balkema) pp 195–206

[16] Thornton C 2000 Numerical simulations of deviatoric shear deformation of granular media *Géotechnique* **50** 43–53
[17] Cundall P A and Strack O D L 1979 A discrete numerical model for granular assemblies *Géotechnique* **29** 47–65
[18] Bashir Y M and Goddard J D 1991 A novel simulation method for the quasi-static mechanics of granular assemblages *J. Rheol.* **35** 849–85
[19] van Baars S 1996 Discrete element analysis of granular materials *PhD Thesis* Technische Universiteit Delft, Delft, Nederlands
[20] Thornton C and Antony S J 2000 Quasi-static deformation of a soft particle system *Powder Technol.* **109** 179–91
[21] Kruyt N P and Rothenburg L 2001 Statistics of the elastic behavior of granular materials *Int. J. Solids Struct.* **38** 4879–99
[22] Luding S, Tykhoniuk R and Tomas J 2003 Anisotropic material behavior in dense, cohesive powders *Chem. Eng. Technol.* **26** 1229–32
[23] Luding S 2004 Molecular dynamics simulations of granular materials *The Physics of Granular Media* ed H Hinrichsen and D E Wolf (Weinheim: Wiley–VCH) pp 299–324
[24] Luding S, Manetsberger K and Müllers J 2005 A discrete model for long time sintering *J. Mech. Phys. Solids* **53** 455–91
[25] Luding S 1998 *Collisions and Contacts Between two Particles* (*Physics of Dry Granular Media—NATO ASI Series E350*) ed H J Herrmann, J-P Hovi and S Luding (Dordrecht: Kluwer) p 285
[26] Walton O R and Braun R L 1986 Viscosity, granular-temperature, and stress calculations for shearing assemblies of inelastic, frictional disks *J. Rheol.* **30** 949–80
[27] Jürgen T 2000 Particle adhesion fundamentals and bulk powder consolidation *KONA* **18** 157–69
[28] Zhu C Y, Shukla A and Sadd M H 1991 Prediction of dynamic contact loads in granular assemblies *J. Appl. Mech.* **58** 341
[29] Sadd M H, Tai Q M and Shukla A 1993 Contact law effects on wave propagation in particulate materials using distinct element modeling *Int. J. Non-Linear Mech.* **28** 251
[30] Brendel L and Dippel S 1998 Lasting contacts in molecular dynamics simulations *Physics of Dry Granular Media* ed H J Herrmann, J-P Hovi and S Luding (Dordrecht: Kluwer) p 313
[31] Luding S, Clément E, Blumen A, Rajchenbach J and Duran J 1994 Anomalous energy dissipation in molecular dynamics simulations of grains: The 'detachment effect' *Phys. Rev.* E **50** 4113
[32] Luding S, Clément E, Blumen A, Rajchenbach J and Duran J 1994 The onset of convection in molecular dynamics simulations of grains *Phys. Rev.* E **50** R1762
[33] Lätzel M, Luding S and Herrmann H J 2000 Macroscopic material properties from quasi-static, microscopic simulations of a two-dimensional shear-cell *Granular Matter* **2** 123–35 (*Preprint* cond-mat/0003180)
[34] Madadi M, Tsoungui O, Lätzel M and Luding S 2004 On the fabric tensor of polydisperse granular media in 2d *Int. J. Solids Struct.* **41** 2563–80
[35] Liao C-L and Chang T-C 1997 A generalized constitutive relation for a randomly packed particle assembly *Comput. Geotech.* **20** 345–63
[36] Kruyt N P and Rothenburg L 1998 Statistical theories for the elastic moduli of two-dimensional assemblies of granular materials *Int. J. Eng. Sci.* **36** 1127–2242
[37] Luding S 2002 Liquid–solid transition in bi-disperse granulates *Adv. Complex Syst.* **4** 379–88
[38] Vermeer P A 1998 *Non-associated Plasticity for Soils, Concrete and Rock* (*Physics of Dry Granular Media—NATO ASI Series E350*) ed H J Herrmann, J-P Hovi and S Luding (Dordrecht: Kluwer)